Journal of Environmental Management 397 (2026) 128208

Contents lists available at ScienceDirect

Journal of Environmental Management

journal homepage: www.elsevier.com/locate/jenvman

Research article

Development of flood detection framework integrating Synthetic Aperture Radar polarimetry and machine learning for semi-urban vegetation systems

Ruma Adhikari, Alok Bhardwaj *

Department of Civil Engineering, Indian Institute of Technology Roorkee, India

ARTICLE INFO

Keywords:
Flood detection
Semi-urban vegetation system
SAR polarimetry
Machine learning

ABSTRACT

Semi-urban vegetation system includes vegetation partly managed by humans and partly growing naturally. It plays a vital role in ecosystem stability but are vulnerable to floods across the world highlighting the need for strategies to enhance resilience to climate change. However, detecting floods is difficult using Earth Observation due to complex scattering between radar signals and varied surface conditions. To address this, Synthetic Aperture Radar (SAR) polarimetry provides information to distinguish scattering patterns of flooded from non-flooded areas. The study proposes a flood detection methodology using Sentinel-1 SAR aimed at combining the Degree of Polarization (DOP) and Linear Polarization Ratio (LPR) derived from Stokes parameters, and Eigenvalues of the SAR covariance matrix. The proposed Flood Index (FI) integrates both amplitude and phase, unlike Normalized Difference Flood Index (NDFI) and VH/VV ratio that use only intensity data; the phase data helps separate smooth flooded surfaces from rough land or vegetation. A Random Forest model trained on the FI with bootstrap sampling detects flood extents accurately in Japan (2019 Typhoon Hagibis), India (2023 Delhi flood), and Greece (2023 Larissa flood). The model achieves F1 scores between 0.81 and 0.86 and Intersection over Union scores between 0.70 and 0.76. The proposed model is better than Otsu and NDFI across all study sites by maintaining lower False Negative Rate (0.09–0.17) and moderate False Positive Rate (0.19–0.39). Better transferability of the trained model is achieved across different flooded areas for scalable flood management in semi-urban vegetation areas.

1. Introduction

Floods are one of the most common and disastrous hazards for semi-urban and agricultural ecosystems across the globe (Schumann, 2024). Semi-urban vegetation system refers to land use land cover in urban-rural fringes that includes vegetation partly managed by humans and partly growing naturally (NVC, 2008). These landscapes, often densely populated and ecologically significant, require robust monitoring to assess flood impacts and support climate resilience. Particularly, South and Southeast Asia including India, Bangladesh, Japan, Vietnam, Laos, and Cambodia experience frequent floods in semi-urban vegetation areas due to storm surges, sea level rise, and tropical cyclones (Subbarayan et al., 2025; Tavakoli et al., 2025). In the last decade, the frequency of extreme floods is reported to have increased by three folds, which is projected to further increase by the end of the mid-21st century (2020–2059) (Phy et al., 2022; Halder et al., 2023; Nayak and Takemi, 2023). For instance, the floods in India, Brazil, UAE, China caused devastating damages of approximately 656 billion USD (Times, 2025). In the near past, Hagibis flood is ranked as the most economically devastating disaster globally in 2019 resulting in a loss of nearly 26 billion USD (CRED, 2020; MLIT, 2021). According to the Intergovernmental Panel on Climate Change (IPCC) 2022, the flooding situation in many Asian countries will worsen in the future highlighting the need for an effective flood disaster management (Tse-Hei Lee, 2020; Portner et al., 2022).

Therefore, mapping and monitoring the floods is essential for faster and effective relief operations (Ermagun et al., 2024), especially in flood prone nations of Asia. Satellite based Earth Observation including both optical and radar remote sensing datasets are a potential way to detect floods accurately (Adhikari et al., 2022). In recent times, multiple spaceborne sensors are available that are operational in visible and microwave bands with different swath widths, spatial resolution, and acquisition geometry. Among all the sensors, Synthetic Aperture Radar (SAR) sensor has the advantage of being operational during day and night as well as during cloud-covered weather conditions (Mehedi et al., 2022, ; Adhikari, 2021; Kumar et al., 2025). Sentinel-1 (C-band), ALOS

* Corresponding author.
E-mail address: alok.bhardwaj@ce.iitr.ac.in (A. Bhardwaj).

https://doi.org/10.1016/j.jenvman.2025.128208
Received 17 July 2025; Received in revised form 10 October 2025; Accepted 1 December 2025
Available online 6 December 2025

PALSAR-2 (L-band), and TerraSAR-X (X-band) SAR sensors are used extensively for flood detection in urban and forested areas (Dasgupta et al., 2018; Tsyganskaya, 2019).

Ideally, fully polarized SAR data is needed for a complete understanding of scattering mechanisms in a flooded area (Pirrone et al., 2020). However, dual-polarized data is frequently available than fully polarized SAR data (Karanam et al., 2021; Garg et al., 2024). Decomposition models based on dual-polarized SAR data fail to provide the "anisotropy" descriptor that quantifies the relative importance between the second and third eigenvalues. For instance, second and third scattering mechanisms (multiple scattering from flooded vegetation, partially flooded urban areas, areas with floating debris and emergent vegetation) are important to detect flood extents. To counter the absence of "anisotropy", we use the Stokes parameters that quantify the polarization state of the received signal. The Stokes parameters are g0, g1, g2, g3, defining total polarized power, power in linear polarization, power in + 45/− 45°, and power in left/right circular polarization, respectively. The Stokes parameters are combined in the Stokes vector for further analysis (Supplementary section B). For Polarimetric descriptors derived from these parameters i.e. Degree of Polarization compensates for the missing anisotropy descriptor (Mandal et al., 2020). Anisotropy and Degree of Polarization (DoP) are similar since both measure the "purity" or "dominance" of scattering mechanisms; anisotropy through eigenvalue balance, and DoP through polarization state purity (Adhikari et al., 2023). Both decrease as scattering becomes more random (Yamaguchi, 2020). For dual-pol data, only DoP is possible to calculate (Mandal et al., 2020). Therefore, in this work, DoP is used in place of "anisotropy" for dual-polarized SAR image available for a flood event.

For effective determination of flood extents, classification methods are used along with polarimetric descriptors obtained from decomposition models. For instance, maximum-likelihood based Wishart classification (Pulvirenti et al., 2016), machine learning classification methods including random forest and support vector machines (Gou et al., 2014; Kazemi Garajeh et al., 2022; Pierdicca et al., 2017), K-Nearest Neighbor (KNN) classifier (Tanim et al., 2022). Recently, U-Net is widely used for SAR data-based flood mapping due to its efficiency with limited labelled SAR data (Fakhri and Gkanatsios, 2025). Some studies have found good performance of Random Forest when compared with U-Net in flood extent mapping (Mandal et al., 2019). Collectively, we find the need of a machine learning based flood detection framework utilizing polarimetric descriptors to detect floods for different LULC classes.

Overall, we find few research gaps in flood detection that we attempt to solve in this work. First, the challenge of separating flooded building producing strong double bounce signals from flooded vegetation with greater depolarization effects. Second, the challenge of detecting flooded vegetation with mixed scattering behavior. Third, the challenge of detection of flooded urban areas. Finally, integrating solutions of aforementioned problems into a machine learning model for rapid flood detection using open-source SAR datasets.

As a solution, first we separate flooded buildings from flooded vegetation by quantifying the relative contribution of surface and double-bounce scattering. Flooded buildings exhibit higher Degree of Polarization (DoP) and lower Linear Polarization Ratio (LPR) due to dominant double-bounce returns, whereas flooded vegetation shows lower DoP and higher LPR resulting from depolarized volume scattering within the canopy. Second, we separate flooded vegetation with mixed scattering from flooded urban areas. We capture non-linear polarization effects caused by multiple scattering within vegetation. We also quantify changes in DoP between pre- and during-flood images to emphasize strong double-bounce reflections from flooded urban regions. Lastly, we propose a machine learning model to handle the proposed flood index derived from eigenvalues of covariance matrix, DoP and LPR. Our proposed method detects floods in different regions without retraining by using physical radar scattering properties and normalization to reduce speckle noise, working well across varied land covers in India, Greece, and Japan.

Therefore, in this work, we propose a Flood Index (FI) developed from polarimetric descriptors including Stokes parameters and Eigen values addressing the aforementioned challenges and proposing a machine learning based framework to detect flood extents in a rapid manner. In Section 1, we discuss the limitations to existing studies. Following this in Section 2, we describe three study areas and datasets. Further in Section 3 we calculate FI for flooded areas for 3 countries i.e. Japan, India and Greece. Next, we propose a Random Forest model trained on FI derived for different flooding events across the world representing different flooded LULC. Finally, in Section 4 we demonstrate that the Stokes parameters and Eigenvalues are able to detect flood extents with enhanced discrimination between different flooded LULC using only the dual-polarized data.

2. Methodology

2.1. Study area and datasets

A world map in Fig. 1 displays global flood occurrence map prepared using the JRC Global Surface Water dataset in Google Earth Engine. On the map, three flood events are shown from Japan, India, and Greece that are used in this work. We consider the study area based on the flood extent, availability of SAR and optical datasets (Table T1 and T2 of the Supplementary section G), and visual inspection on the pre and during flood optical satellite images (Supplementary section G, Fig. S4). For the flood events in India and Greece, all high-resolution optical datasets were fully covered by clouds. PlanetScope (3 m) was the only dataset with few cloud-free patches, matching SAR acquisition time, where flooded areas were visible in India and Greece. Moreover, the study sites had broad land cover units (large fields, wider floodplains, and less fragmented land use), which made the coarser PlanetScope imagery sufficient for distinguishing flooded from non-flooded areas and preparation of labels. Whereas, the Nakashi area in Japan has a complex landscape with fine-scale land cover patterns, such as narrow rivers, paddy fields, and dense urban features. To accurately separate water from such detailed surroundings, higher spatial resolution was needed. Therefore, SPOT-6 (1.5 m) was used, as PlanetScope's 3 m resolution would not have captured the small-scale flooded features distinctly. Optical satellite images of flooded region in Japan, India, and Greece are shown in Supplementary section F.

2.1.1. Japan

The typhoon Hagibis that made landfall in the Ibaraki Prefecture of Japan on October 12 (JST), 2019 is now considered as one of the most powerful typhoons to have occurred in Japan resulting in widespread floods and landslides (Das et al., 2020). Tay et al. (2020) reported that the Naka River as shown in Fig. 1(1), which flows through the Ibaraki Prefecture, was flooded resulting in the inundation of over 80,000 houses and a large portion of agricultural land causing economic losses of over 27 billion USD. As mentioned by Fu et al. (2021), the data from the Hitachi-Omiya observation station of the AMeDAS (Automated Meteorological Data Acquisition System) shows the peak water levels (11.4 m and 2.7 m) at stations named as N2, N3 respectively on the Naka riverbed, which caused an overflow at these locations. Flooded area includes port area (mid-urban) to the N2 station, Red cross hospital, Ibaraki university, agricultural fields with scattered settlements.

2.1.2. India

A major rainfall induced flood occurred in the Delhi NCR (National Capital Region) of India between July 8 to 13, 2023 (Soudagar et al., 2025). The water level reached 208.66 m in the Yamuna river (FloodList, 2023). Several low-lying areas along the river flood plain were flooded including human settlements and agricultural land. We select our study area by considering the extent of the flooding, and available Sentinel-1 and optical datasets.

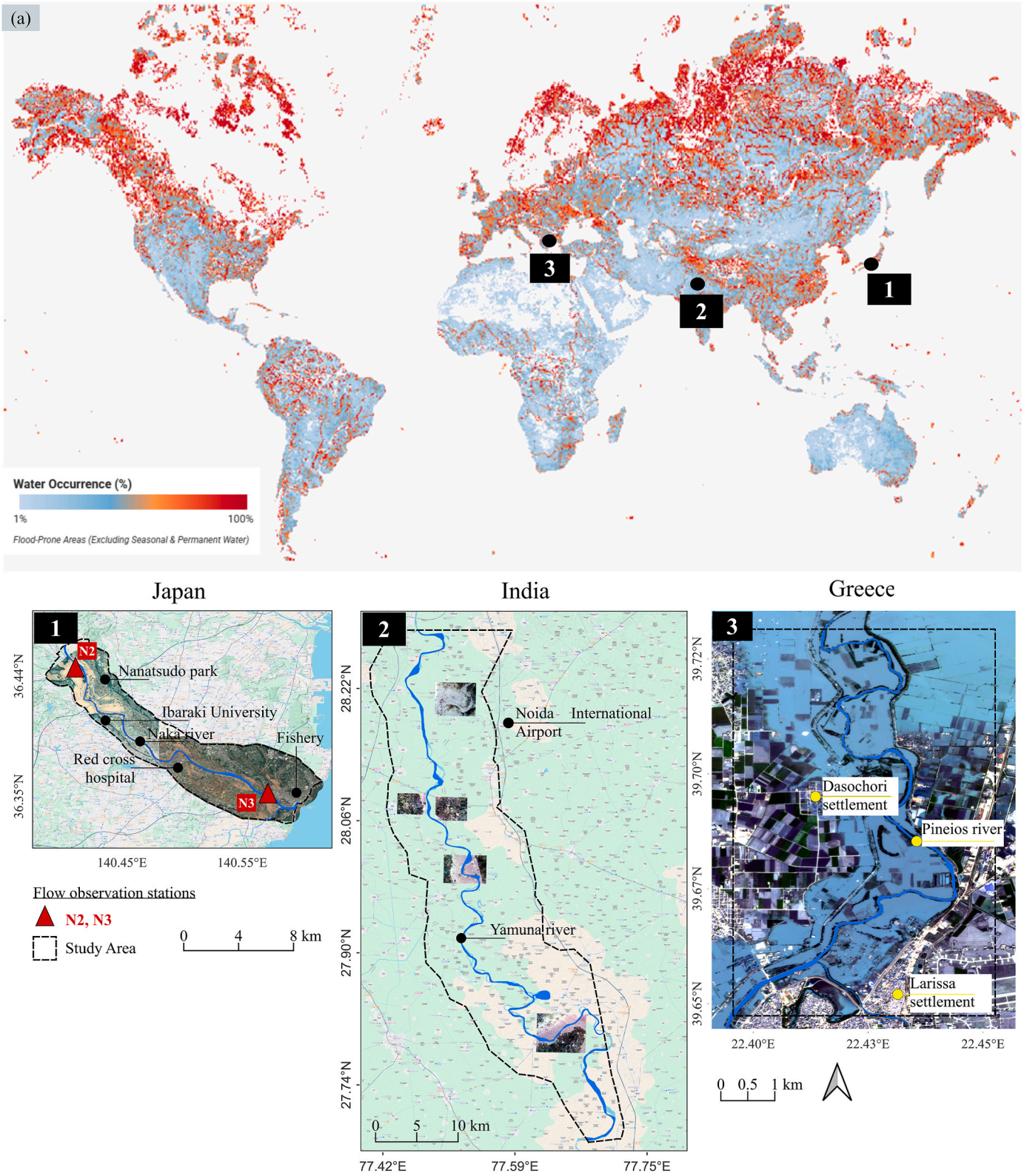

Fig. 1. (a) World map showing the global flood occurrence dataset spanning 38 years from March 1984 to December 2021, created by analysing 4.4 million Landsat 5, 7, and 8 satellite images at 30-m resolution to indicate flood frequency patterns worldwide (Pekel et al., 2016). Study areas from three countries: (1) Region from Japan surrounding the Naka River in Ibaraki prefecture, which covers two flow observations stations N2 and N3, and important locations including hospital, university, parks, and agricultural lands in the vicinity of the Naka river; (2) Region from India surrounding the Yamuna river in Delhi NCR; (3) Region from Greece surrounding the Pineios river at Larissa area.

2.1.3. Greece

A major torrential rainfall event occurred in Greece in 2023 that caused a major flood in the region of Larissa (CBS, 2023). The area in the vicinity of the Pineios river was inundated by flood water that caused large damage to infrastructure including part of the Athens-Thessaloniki highway. The study area in Greece is selected based on the similar acquisition time of Sentinel-1 and optical datasets as shown in Supplementary Table T1 and T2, respectively.

3. Methods

We describe a methodology to process Sentinel-1 SLC data to obtain polarimetric descriptors the degree of polarization and linear polarization ratio, which are used for proposing the Flood Index. Next, we describe the Random Forest model that is trained on the Flood index and compared with standard methods of Otsu (1979) and NDFI to detect flood extents for three study areas.

3.1. Geolocation uncertainty analysis between SAR and optical images

To assess the geolocation uncertainty between Sentinel-1 and PlanetScope, we measured Root Mean Square Error (RMSE) and Mean Absolute Error (MAE) at independent Ground Control Points, such as road intersections and building corners. The detailed explanation to minimize geolocation uncertainty is included in the Supplementary section D. After DEM-based orthorectification, the residual misalignment RMSE and MAE were obtained as 3.970 m and 3.795 m, respectively. This is less than the resampled Sentinel-1-pixel size of 5m, confirming minimal uncertainty (as discussed in Supplementary section D).

3.2. Pre-processing of Sentinel-1 SLC data

The pre-processing of raw data is crucial to generate a geocoded polarimetric 2 x 2 covariance matrix (C2). As shown in the flowchart in Fig. 2, the Terrain Observation with Progressive Scans SAR (TOPSAR)

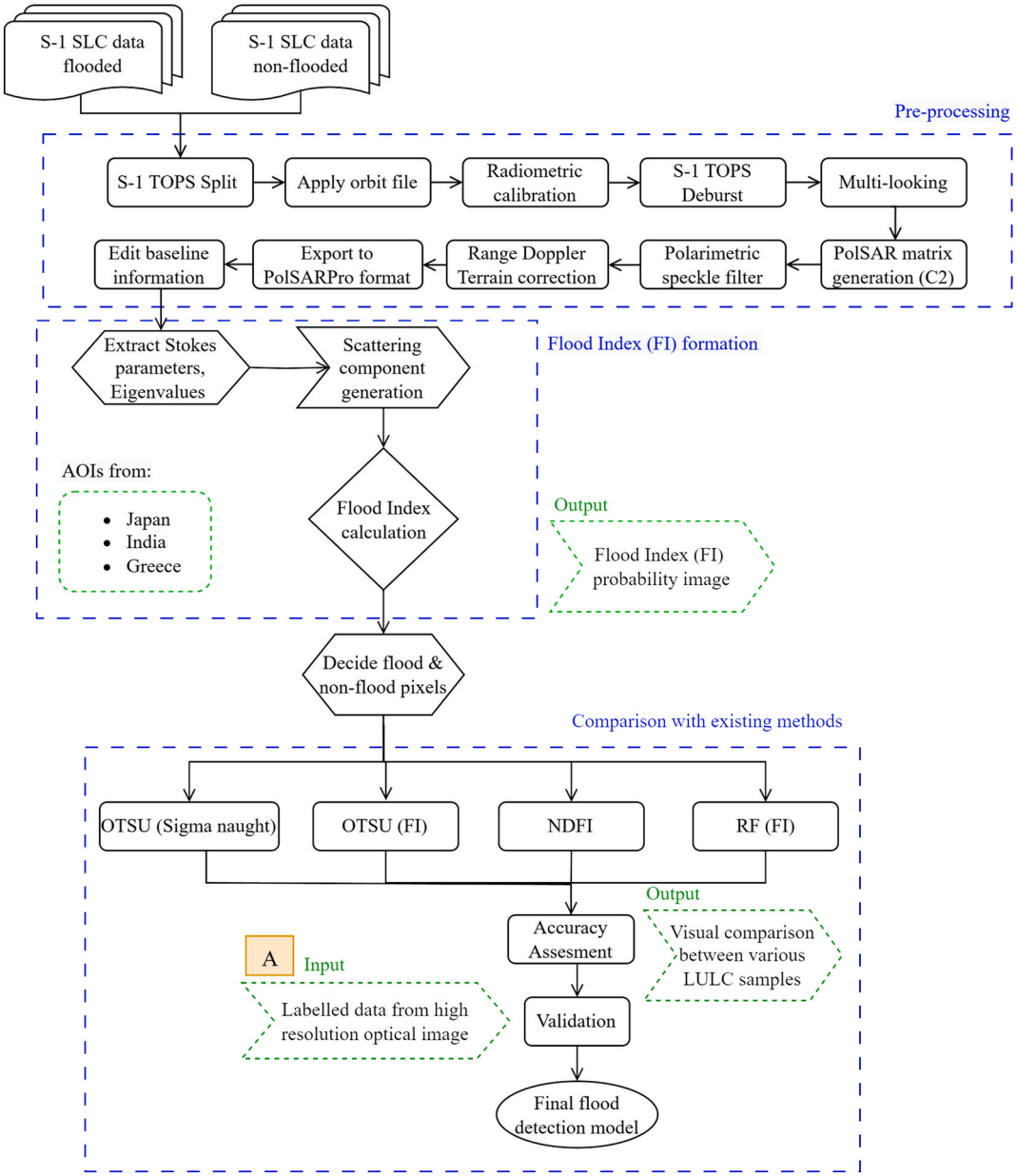

Fig. 2. The detailed flowchart of the methodology adopted in the study including the pre-processing of the Sentinel-1 data, extraction of polarimetric descriptors, development of Flood Index (FI), machine learning model training on the FI, comparison of trained model on FI with existing methods, and accuracy assessment.

split is applied to select the intended burst before assigning precise orbit information to the data. The radiometric calibration corrects for variations in the radar instrument's sensitivity, ensuring that pixel values consistently represent radar backscatter values. Next, a deburst operation is applied to obtain a continuous image from the signal (Supplementary section E).

The multi-looking operation reduces the spatial resolution for both the range and azimuth directions with additional noise cancellation. The final product is used to generate a polarimetric covariance matrix (C2) based on the Pauli vector. A Lee Refined filter is applied followed by terrain correction with 30 m SRTM DEM (Farr et al., 2007) for reducing signal clutter that leads to salt and pepper grainy texture in SAR images (Mandal et al., 2019).

3.3. Polarimetric parameters

After the pre-processing in the SNAP software, the Stokes parameters are obtained. The Stokes parameters are g0, g1, g2, g3, defining total polarized power, power in linear polarization, power in + 45/− 45°, and power in left/right circular polarization, respectively. The Stokes parameter are related to each other as per Equation (6) of the Supplementary section B and are used to calculate Degree of Polarization (DOP), denoted by symbol 'm' (Supplementary section Equation (7)), and Linear Polarization Ratio (LPR) denoted by symbol 'μ_L' (Supplementary section Equation (8)). Next, Eigenvalues (EV_1, EV_2) are calculated from the covariance matrix of the Sentinel-1 data using the PolSARPro software (Supplementary section Equations (10)–(12)).

The DOP is a measure of the polarization purity of a radar signal. It quantifies the degree of polarization of the received signal. The LPR is a measure of the ratio of the magnitude of linearly polarized radar returns to the total radar return, which includes both linearly and circularly polarized components. It occurs when the orientation of the scattering structures within a scene aligns with the linear polarization states of the transmitted radar signal. DOP and LPR are less sensitive to absolute magnitudes of received signal and provides comprehensive insight into the complex scattering processes in a flooded area (Felix et al., 2024).

We calculate the DOP and LPR for all the study sites (Japan, India, Greece) for pre-flood and during flood dates. Here, we show the analysis of DOP and LPR for Japan, whereas the DOP and LPR data for

Next, we calculate the sum of EV_1 and EV_2 to consider scattering properties from every type of flooded LULC and use it as weights for DOP and LPR to highlight dominant scattering while preserving physical characteristics represented by Eigenvalues. We have used EV_1 and EV_2 since the covariance matrix has a rank of 2 for dual-pol Sentinel-1 data. The DOP and LPR are shown as follows (Eq. (1) & Eq. (2)) (Mandal et al., 2020):

$$M_{pre} = EV_{pre} \ x \ m_{pre} \tag{1}$$

$$M_{during} = EV_{during} \ x \ m_{during} \tag{2}$$

where,

$$EV_{pre} = (EV_1 + EV_2)$$

Where EV_{pre} is sum of the eigenvalues (EV_1, EV_2) from pre-flood condition and m_{pre} is the degree of polarization for pre-flood data. Similarly, EV_{during} and m_{during} denote Eigenvalue and DOP during the flood, respectively. In the case of dual-pol (C2) data, the covariance matrix has rank 2 and thus only two non-zero eigenvalues (EV_1, EV_2), while the third pseudo-eigenvalue is identically zero by definition.

In a similar way, $\mu_{L_{pre}}$ and $\mu_{L_{during}}$ are calculated. Further, weighted DOP and LPR are normalized as follows:

$$M_N = \frac{M_{pre} - M_{during}}{M_{pre} + M_{during}} \tag{3}$$

$$\mu_{L\_N} = \frac{\mu_{Lpre} - \mu_{Lduring}}{\mu_{Lpre} + \mu_{Lduring}} \tag{4}$$

3.4. Flood index (FI) formation

Flood Index (FI) is developed using normalized Degree of Polarization and normalized Linear polarization ratio that comprises of three components. The first component of FI highlights the difference between normalized DOP and LPR to detect flooded buildings and flooded vegetation. The second component enhances the detection of flooded vegetation due to multiple scattering, and the third component captures the scattering information from flooded buildings using DOP. The FI is obtained through multiplication of the three components since SAR backscatter follows multiplicative behavior enabling accurate representation of complex scattering mechanisms by preserving the characteristics of the backscattered wave (Guissard, 1994; Skolnik, 2014).

Since the FI is based on dual-pol SAR data (e.g. Sentinel-1) for its simplicity in application, we explain the flooded vegetation and flooded urban scattering mechanisms in terms of the Stokes parameters pictorially in Fig. 3 that are included in the derivation of the FI. For instance, during floods partially submerged vegetation creates random scattering increasing DOP whereas completely submerged vegetation increases surface scattering causing higher LPR and lower DOP. For flooded urban areas, slight increase in LPR and larger increase in DOP is caused due to increased surface scattering and double bounce scattering mechanism.

3.4.1. Uncertainty sources

In flooded vegetation, several mechanisms effect radar backscatter. First, partially submerged vegetation causes random scattering, reducing the degree of polarization (DOP). Second, canopy interception occurs when C-band radar signals mainly reflect off the upper plant canopy, limiting interaction with the water surface below. Third, the absorption impact from water, which has a high dielectric constant, reduces the returned signal by absorbing more energy. Lastly, modified surface interaction arises when submerged vegetation enhances surface scattering (reflected more strongly), but reduces randomness in scattering, again lowering the DOP. In urban flooding, radar behaves differently due to man-made structures. Surface scattering increases when floodwaters cover buildings, enhancing the linear polarization ratio (LPR). Corner reflection occurs when water forms ideal conditions for double-bounce reflections between building walls and the ground, increasing both DOP and signal strength. Material enhancement also plays a role, as highly reflective urban surfaces (like concrete or metal) create stronger radar echoes. Finally, signal pathway efficiency improves in flooded areas due to less absorption and more multiple-bounce paths, which amplify the return signal.

3.4.2. Calculation of the first component of the flood index

In flooded urban areas, where double-bounce scattering dominates, LPR is lower, and DOP is higher due to strong return in both HH and VV channels leading to a smaller difference between the two Stokes parameters. In contrast, flooded vegetation exhibits a slightly higher LPR, and lower DOP compared to flooded buildings due to volume scattering within the vegetation canopy that tends to depolarize the signal. This reduces the difference between HH and VV channels.

To discriminate between flooded buildings and flooded vegetation by quantifying the relative response of surface scattering, normalized LPR and normalized DOP are combined through multiplication as shown in Equation (5).

$$\text{Flood Index (FI\_1)} = (m_N * \mu_{L\_N}) \tag{5}$$

Further, the multiplication makes the output sensitive to extreme values so that FI_1 captures large changes in the $(M_{pre} - M_{during})$ and $(\mu_{Lpre} - \mu_{Lduring})$ due to flood.

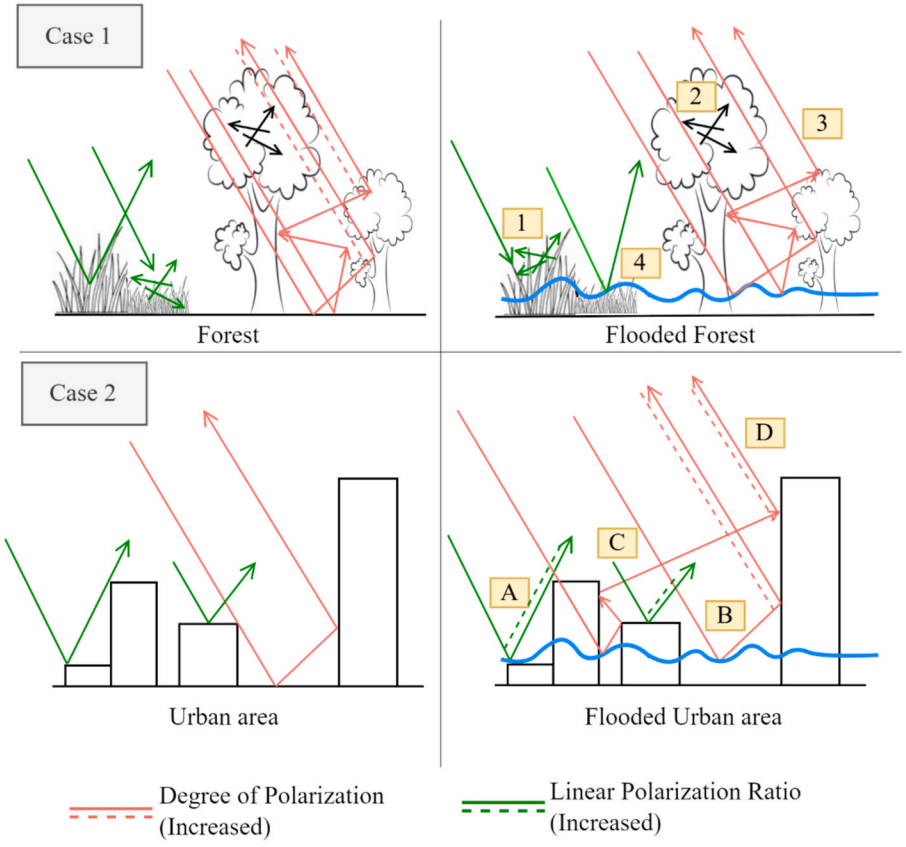

Case 1 **Flooded Vegetation Scattering Mechanisms**:

1 *Depolarization Effect*: Partially submerged vegetation creates random scattering, reducing DOP

2 *Canopy Interception*: C-band signals scattered by upper canopy, limited water surface interaction

3 *Absorption Impact*: High water dielectric constant increases signal absorption, reduces return

4 *Modified Surface Interaction*: Submerged vegetation increases surface scattering (higher LPR), decreases random scattering (lower DOP)

Case 2 **Urban Flood Scattering Mechanisms**:

A *Surface Scattering*: Flooded structures increase surface scattering with moderate LPR enhancement

B *Corner Reflection*: Water creates ideal corner reflector geometry, enhancing double bounce and DOP

C *Material Enhancement*: High reflectivity urban materials produce stronger specular reflections

D *Signal Pathway Efficiency*: Reduced absorption and multiple bounce pathways amplify return signal

(caption on next page)

Fig. 3. Signal attenuation in presence of flood water in two LULC types i.e. Vegetation and Urban. Case 1 shows increase in linear polarization ratio due to volume scattering in partially flooded vegetation and decrease in degree of polarization due to multiple scattering that leads to weaker backscatter signal. A decrease in linear polarization ratio is observed for fully submerged vegetation. Case 2 shows moderate increase in linear polarization ratio due to wet surface of buildings and high-level increase of degree of polarization due to double bounce scattering which leads to stronger backscatter signal.

3.4.3. Calculation of the second component of the flood index

A major challenge in flood water detection is to identify the mixed scattering component from various types of flooded vegetation (Brisco et al., 2013; Plank et al., 2017). This includes wetlands with emergent vegetation, flooded paddy field and sediment water that cause multiple scattering leading to non-linear polarization. The non-linear polarization occurs due to wave transformation from linear to elliptical or circular polarization through multiple interactions. The non-linear polarization can be quantified by subtracting the linear polarized power from the degree of polarization (i.e., $m_N - \mu_{L\_N}$).

This difference between normalized DOP and normalized LPR is multiplied with FI_1 to calculate the second component of FI_2 as follows:

$$\text{Flood Index (FI\_2)} = (m_N * \mu_{L\_N}) * (1 + |m_N - \mu_{L\_N}|) \quad (6)$$

Since $(m_N - \mu_{L\_N})$ can be zero due to similar values, we added 1 to the difference to avoid FI_2 becoming zero.

3.4.4. Calculation of the third component of the flood index

The third component of the Flood Index differentiates flooded urban areas from other targets. Flooded buildings exhibit enhanced double-bounce returns during floods whereas backscatter from other targets such as partially submerged vegetation is variable (Mason et al., 2014). The increased double-bounce component of flooded buildings can be quantified by calculating the difference of Eigenvalue weighted DOP of pre-flood date from during flood date $(M_{during} - M_{pre})$. Although the difference falls on an infinite scale, it is useful when the first two components might become diminutive. This approach also allows greater influence for a small change in the Eigenvalue weighted DOP $(M_{during} - M_{pre})$. Further, we calculate the absolute value of the difference $(|M_{during} - M_{pre}|)$ to only extract the positive change indicating increase in backscattering magnitude. This approach effectively excludes the case when DOP decreases for smooth surfaces. In situations when 'M' shows a negative change $(M_{pre} > M_{during})$, the overall value becomes zero. For the case when $M_{during} > M_{pre}$, we divide the total changed value by 2. Additionally, we implement a unitary summation of this component to ensure that when the output is zero, it does not nullify the entire FI calculation. The resulting component can be expressed as follows:

$$FI\_3 = 1 + \frac{(M_{during} - M_{pre}) + |M_{during} - M_{pre}|}{2} \quad (7)$$

Finally, the third component is multiplied with the output from our second component (Eq. (6)) to give the final Flood Index (FI_F) as follows:

$$\text{Flood Index Final (FI\_F)} = \left[(m_N * \mu_{L_N}) * (1 + |m_N - \mu_{L_N}|)\right] * \left[1 + \frac{(M_{during} - M_{pre}) + |M_{during} - M_{pre}|}{2}\right] \quad (8)$$

We performed sensitivity analysis to understand the effect of noise on FI_1, FI_2 and FI_3, since the proposed index should remain stable under different speckle noise conditions. Specifically, we perturbed DoP and LPR by ± 5 % to simulate speckle noise conditions. Next, we calculated mean and standard deviation of FI_1, FI_2 and FI_3 for different combinations of perturbed DoP and LPR. We observed no influence of perturbations on the flood indices, indicating robustness to speckle noise in detecting flood extents. The detailed sensitivity analysis is included in the Supplementary section M.

Additionally, we perform an ablation study on the proposed flood index (FI_F) that shows the sensitivity of the FI_F to the contributing individual flood index components (FI_1, FI_2, FI_3). Specifically, we compared different combinations: FI_1 × FI_2, FI_1× FI_3, FI_2× FI_3 with FI_F (FI_1× FI_2× FI_3) for flooded urban and flooded vegetation areas. The detailed analysis is included in the Supplementary section N. We found that FI_F produces the most balanced detection with continuous flood patches, reduced false alarms, and better separation of flooded and non-flooded areas without over-estimating flood extents.

For visual inspection of the performance of the three components of the Flood Index in detecting flood extents, we selected flooded urban, flooded vegetation and flooded sediment areas from Japan (Fig. 4 & Supplementary section K, Figs. S17–S19). For the flooded urban area (Fig. 4), we observe a significant improvement in the detection of flooded buildings from the first to the final index. FI_2 captures non-linear polarized backscatter more effectively than FI_1, particularly from vegetation and buildings oriented across the antenna's line of sight. This allows FI_2 to better detect flooded buildings with such orientations. FI_3 further enhances detection by capturing increased backscatter from partially flooded buildings. In Fig. 4, the red circles highlight improved signal detection for flooded buildings from FI_1 to the final index FI_F.

For the flooded agricultural area (Fig. 4), we observe improvement in detection of flooded vegetation from FI_1 to FI_2 since FI_2 can capture multiple scatterings from different types of vegetation. The brighter pixels in FI_2 show fully submerged agriculture fields, improving contrast between water and flooded vegetation. FI_2 and FI_F look similar since FI_F is designed to identify flooded buildings along with flooded vegetation, but there are few flooded buildings in the examples shown in Fig. 4. Similarly, for test tile 5, FI_2 shows better delineation of flooded vegetation. FI_F identifies some flooded buildings as well, since FI_F is designed to detect both flooded vegetation and flooded buildings.

As discussed in Supplementary Section L, we calculate the probability density plots for the three LULC classes, which shows development of the Flood Indices in three stages. The analyses compare the performance of three flood indices (FI_1, FI_2, FI_F) across different land cover types - urban, vegetation, and mixed urban & vegetation. A rightward shift and sharper peaks in FI_F consistently show improved flood detection accuracy in all the three LULC Test Tiles samples. The final Flood Index (FI_F) output for the three study areas, i.e. Japan, India, and Greece are shown in Fig. 5. The values range from 0 (low) to 1 (high). A higher value (shown in blue) implies the pixel is more likely to be flooded, while a lower value (shown in red) indicates the area is less likely to be flooded.

3.4.5. Proposed random forest (RF) model

Polarimetric parameters are often correlated and show non-linearity between radar signal and polarimetric descriptors (Wang et al., 2019). Moreover, flood areas exhibit a complex phenomenon with partially submerged man-made features and vegetation, resulting in a mixed aggregate of low and high backscatter returns that are difficult to distinguish from non-flooded high backscatter values. We, therefore, use the ensemble machine learning method of Random Forest (RF) (L. Breiman et al., 1984) to separate backscatter information from flooded urban and flooded vegetation areas. We collate training and test tiles from all the three study areas, Japan (Fig. 4), India, and Greece (Supplementary Figs. S28 and S29). The TEST Tiles are shown in red in Fig. 4, Figs. S28 and S29. The tile-based data sampling approach for handling data imbalance between flood and non-flood class pixels for training RF models is discussed in the Supplementary section Q and

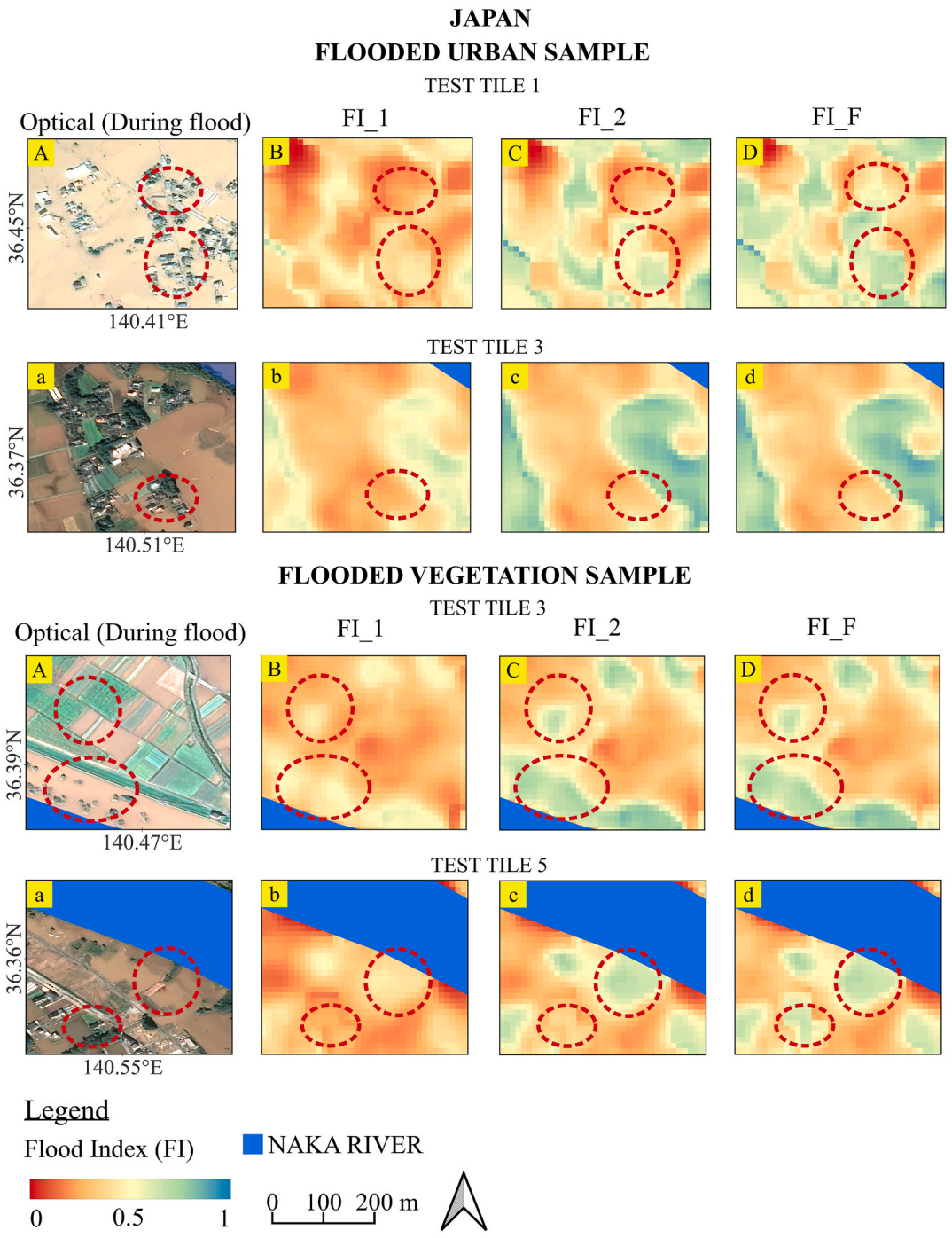

Fig. 4. Comparison of Flood Indices (FI) in Japan for two Flooded Urban and Vegetation Samples: (A)&(a) High-resolution during-flood Optical image; (B)&(b) Flood Index output from first component (FI_1); (C)&(c) Flood Index output from second component (FI_2); (D)&(d) Final Flood Index (FI_F = FI_1 x FI_2 x FI_3). More detail on test tiles 1, 2, and 5 is shown in Fig. 5A.

Fig. S30. Next, we split the sampled data into 80 % Training and 20 % Validation data. We evaluate the top 20 Random Forest models with the lowest Out-Of-Bag score (as shown in Supplementary Table T5). Among these top models, we select the best-trained model based on the accuracy metric on the validation dataset.

We also estimated the average time for each test tile prediction as 13 s that will assist in effective disaster response [Supplementary section Q (i)].

4. Results & discussions

We present results on the application of the Random Forest (RF) model on the proposed Flood Index (FI_F) and compare it with established flood detection methods of Otsu thresholding on sigma naught backscatter obtained from Sentinel 1 for flood dates across Japan, India, and Greece, and Normalized Difference Flood Index (NDFI) (Cian et al., 2018). The details of Otsu and NDFI are given in Supplementary Sections J and K. We also apply Otsu thresholding on the proposed FI_F and compare with the other methods of flood detection.

Overall, across all the three study regions, the FI(RF) demonstrates

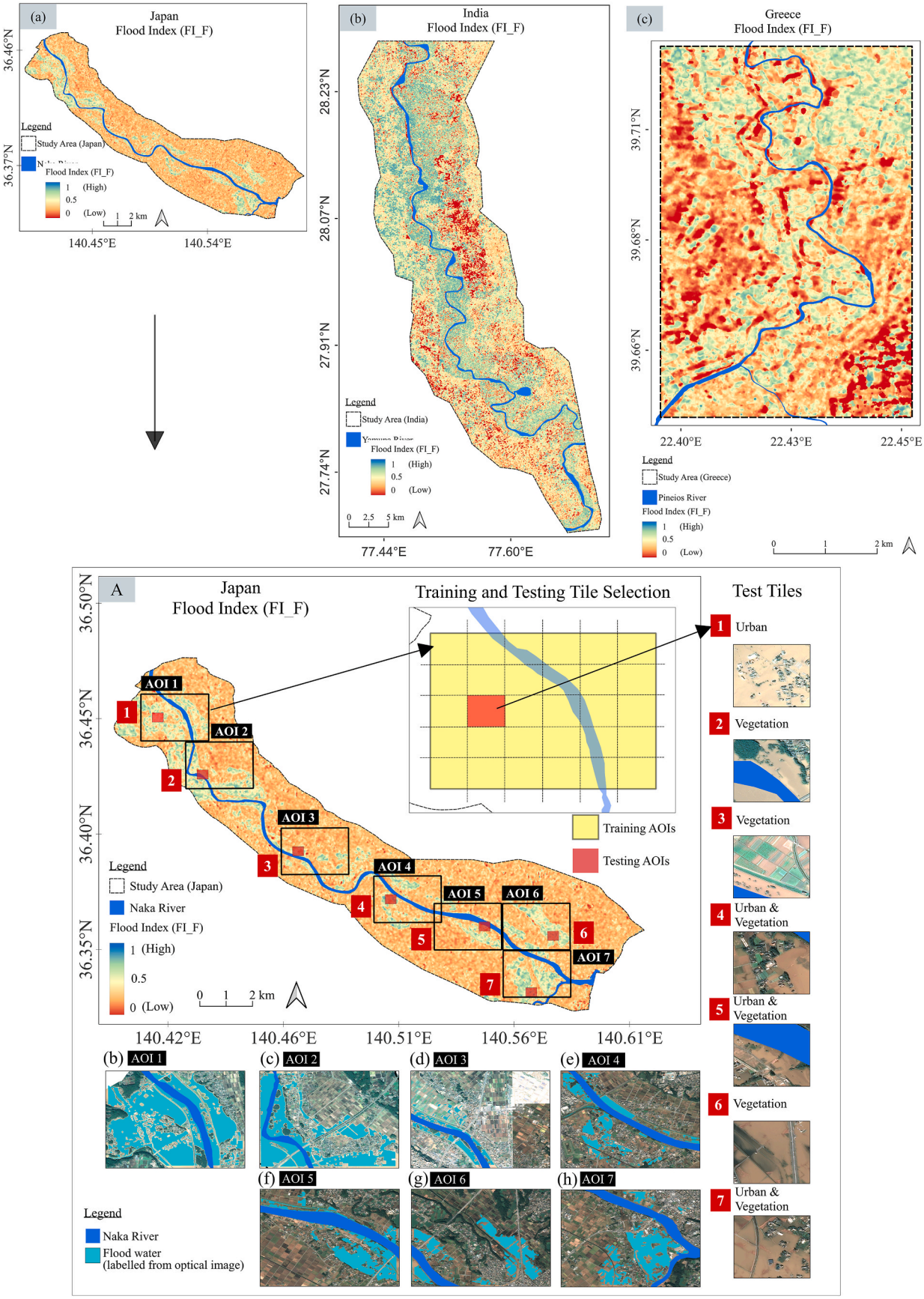

Fig. 5. Flood Indices (FI_F) for: (a) Japan (b) India (c) Greece. Blue color indicates the area is more likely to be flooded and red color indicates the opposite. (A) Seven AOIs shown for Japan. Test tiles are selected from all AOIs. All AOIs except test tiles are used for training. Optical images with flood extents are shown for each AOI. Optical images for flooded urban and flooded vegetation test tiles are shown. Base map of study area shows Flood Index (FI_F; Eq. (10)).

the highest accuracy in detecting flooded urban areas, particularly in Japan (tile 1), India (tiles 1 and 5), and Greece (tile 2). The method also shows high accuracy in detecting flooded vegetation (excluding agriculture areas) in Japan (tile 2), India (tiles 2 and 4), and Greece (tiles 1 and 4). In contrast, flood water detection in agricultural areas remains a challenge due to the limitation of the C-band dual-polarized SAR data to penetrate the canopy and thus providing limited polarimetric information in agricultural areas. Next, we show the visual assessment of all the methods over the flooded urban and flooded vegetation areas in Japan, India, and Greece (Figs. S27–S28). The labels are white for flooded areas and black for non-flooded areas.

4.1. Japan

In Fig. 6, we show the application of the four methods on flooded urban test tiles 1 and 4 and flooded vegetation test tiles 3 and 5 in Japan. The RF (FI_F) shows the most accurate detection of flood boundary for both flooded urban and flooded vegetation test tiles. Otsu (FI_F) and Otsu (Sigma naught) perform similarly in urban areas. But, for flooded vegetation areas, Otsu (FI_F) shows slightly higher false negatives and Otsu (Sigma naught) shows slightly higher false positives, as indicated in Supplementary Fig. S34. NDFI shows higher false negatives by not detecting floods in both flooded urban and vegetation test tiles.

4.2. India

Fig. 7 shows the flooded urban test tiles 1 and 5 and flooded vegetation test tiles 4 and 6 for India. Urban tiles depict flooded settlements with agriculture surrounded by flood water, unlike flood water within buildings as in Japan. We observe both the Otsu (Sigma naught) and RF (FI_F) detect the flood boundaries better than the other two methods for tiles 1 and 5. For vegetation tile 4, we observe that Otsu (Sigma naught) and Otsu (FI_F) has a higher FPR (0.78 and 0.79, respectively, Fig. S34) indicating that Otsu method is not able to detect flooded vegetation. RF (FI_F) has both lower FPR and FNR (0.50 and 0.11, respectively, Fig. S34) showing it is successful in detecting flooded vegetation.

For tile 6, RF (FI_F) shows higher FPR (0.54, Fig. S34), whereas Otsu (Sigma naught) and NDFI shows a better prediction of flood due to lower FPR. However, NDFI has a slightly higher FNR for tile 6. Otsu, however, detects existing river as flood. RF(FI_F) identifies few non-flooded agriculture plots as flood that are located within settlement areas, which could be due to wetting of the agriculture crops with similar backscatter signature to that of flooded vegetation surrounded by flood water and are not located within settlement areas.

4.3. Greece

Fig. 8 shows flooded urban test tiles 2 and 5 and flooded vegetation test tiles 1 and 3 for Greece. For flooded urban test tile 2, RF (FI_F) has the least number of false positives and false negatives, followed by Otsu (Sigma naught). Otsu (FI_F) and NDFI fails to predict flood extents accurately due to higher false positives for Otsu (FI_F) and higher false positives and false negatives for NDFI (Fig. S34). Similarly, for test tile 5, RF (FI_F) performs the best due to lower FPR and FNR. However, NDFI shows higher false negatives, and Otsu (sigma naught) shows higher false positives. This could be attributed to the complex scattering from

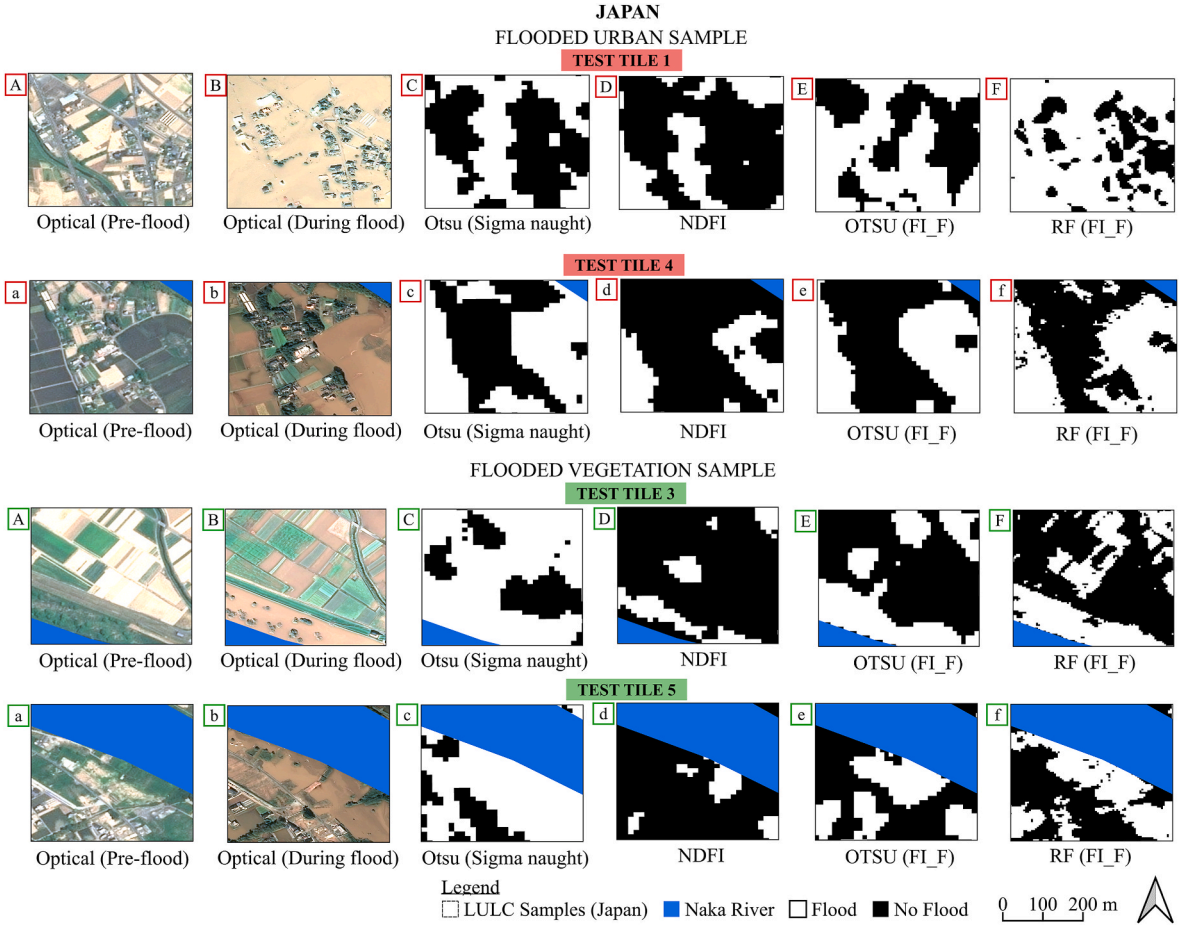

Fig. 6. Flooded Urban test tiles 1 and 4 and Flooded Vegetation test tiles 3 and 5 in Japan. Flood detection using the four methods: (A) and (a) Optical imagery before the flood (SPOT 6, 1.5 m spatial resolution); (B) and (b) Optical imagery during the flood (Pleiades, 50 cm spatial resolution); (C) and (c) Otsu (Sigma naught); (D) and (d) NDFI; (E) and (e) Otsu (FI_F); (F) and (f) Random Forest (FI_F). The labels are white for flooded areas and black for non-flooded areas.

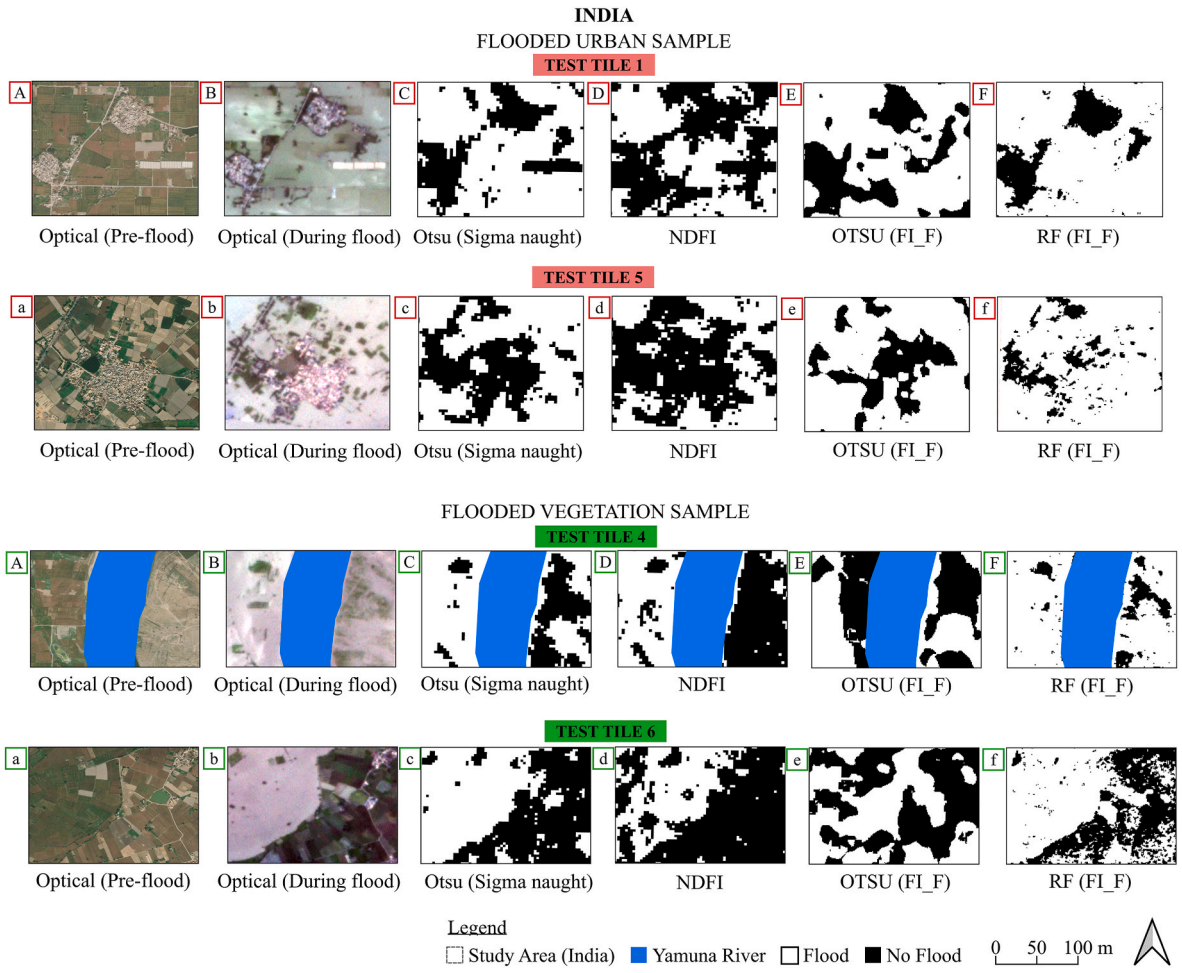

Fig. 7. Flooded Urban test tiles 1 and 5 and Flooded Vegetation test tiles 4 and 6 in India. Flood detection using the four methods: (A) and (a) Optical imagery before the flood (PlanetRGB, 3 m spatial resolution); (B) and (b) Optical imagery during the flood (PlanetRGB, 3 m spatial resolution); (C) and (c) Otsu (Sigma naught); (D) and (d) NDFI; (E) and (e) Otsu (FI_F); (F) and (f) Random Forest (FI_F). The labels are white for flooded areas and black for non-flooded areas.

flooded areas from a dense mix of urban and vegetation land cover where features are randomly oriented in test tile 5 as shown in Fig. 8. RF (FI_F) successfully detects scattered flooded pixels in between buildings and vegetation. For flooded vegetation test tiles 1 and 3, RF (FI_F) consistently shows higher F1 scores with lower FPR and FNR. Otsu (sigma naught) predicts flood extents with good accuracy for tile 1 but underperforms for tile 3 due to higher value of false positives in the vicinity of non-flooded vegetation. Otsu (FI_F) reports higher number of false negatives for both tiles 1 and 3. NDFI performs the least with the highest number of false negatives for both the tiles 1 and 3, incorrectly indicating absence of floods.

Collectively, random forest model trained on the proposed flood index performs the best across all the study areas with consistently good accuracy to predict flood extents across flooded urban and flooded vegetation class. The inaccurate results of RF (FI_F) are attributed to the limitations of dual-pol data in identifying different polarimetric scattering in flooded areas. Another limitation of the C band signal since is its inability to detect flood water under the canopy of the trees.

In agriculture tile 6 (India), FI mislabels wet but unflooded cropland as flooded due to similar backscatter from moist soils. Microwave backscatter in SAR is strongly influenced by the dielectric constant of the target. Water has a very high dielectric constant (~80) compared to dry soil (~3–5). When cropland is wet or irrigated, the higher dielectric values of soil increases the radar return and alters the scattering in a way that resembles inundated surfaces (Elkharrouba et al., 2022). In C-band SAR, where penetration into the canopy is limited, this effect is more pronounced because both wet soil beneath crops and shallow floodwater beneath vegetation give similar signatures (B. Zhang et al., 2022). As a result, the Flood Index (FI) incorrectly interprets wet cropland as flooded, since the sensor "sees" the high dielectric contrast caused by moisture but cannot separate whether it comes from soil wetness or actual standing water. Potential solutions include using temporal coherence, longer-wavelength SAR, or texture features to better separate wet fields from floods (Sghaier, 2018). A possible solution is to check stability of temporal coherence from longer-wavelength SAR (e.g., L-band) data since L-band provides better penetration through crops and represent texture features that capture spatial context and help distinguish between true floodwater from wet agricultural fields.

Flood detection under vegetation is challenging because mixed scattering from wetlands, paddy fields, and sediment-laden water produces non-linear polarization. Intensity-based Otsu methods fail to capture these conditions, as thresholding a single backscatter distribution cannot separate mixed scattering from flood signals. Similarly, Otsu applied on the Flood Index improves performance but still struggles with class variability across different flooded land cover types. The Normalized Difference Flood Index (NDFI) also shows poor generalization, as spectral contrasts between water and other targets become ambiguous under vegetation or sediment-laden conditions. The second Flood Index component addresses the vegetation-related challenge by capturing mixed scattering effects, while the third component differentiates flooded urban areas by exploiting double-bounce signatures. The comparative results confirm these advances: while Otsu- and NDFI-based

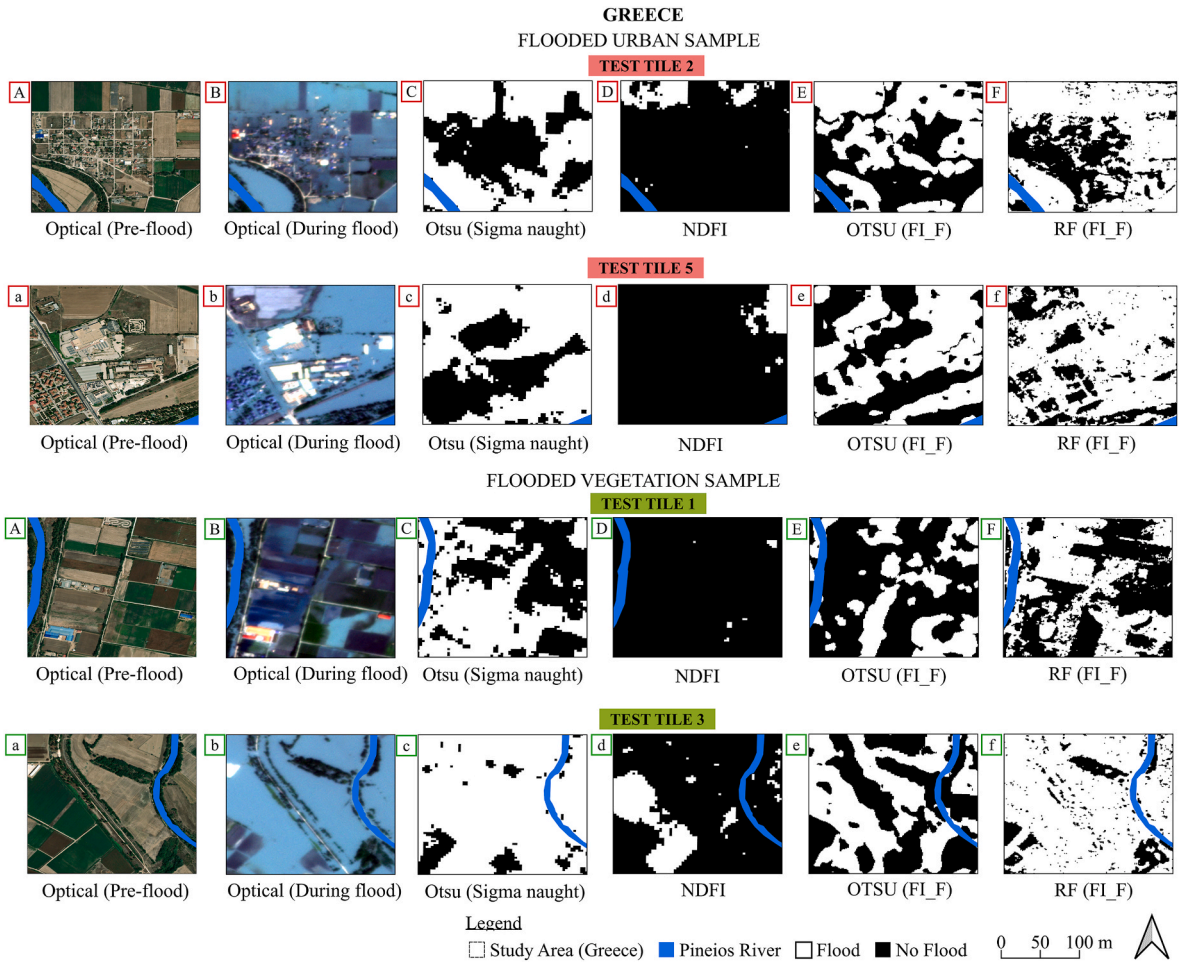

Fig. 8. Flooded Urban test tiles 2 and 5 and Flooded Vegetation test tiles 1 and 3 in Greece. Flood detection using the four methods: (A) and (a) Optical imagery before the flood (PlanetRGB, 3 m spatial resolution); (B) and (b) Optical imagery during the flood (PlanetRGB, 3 m spatial resolution); (C) and (c) Otsu (Sigma naught); (D) and (d) NDFI; (E) and (e) Otsu (FI_F); (F) and (f) Random Forest (FI_F). The labels are white for flooded areas and black for non-flooded areas.

methods yield lower F1 and IoU and higher FNR, RF(FI) consistently achieves higher F1 (0.81–0.86) and IoU (0.70–0.76), with the lowest FNR across all study sites (Supplementary Section R, Fig. S34), demonstrating that the learning-based approach effectively resolves the limitations of threshold-based methods.

Further, we perform a 3-fold cross validation among the three study sites to assess the model performance on unseen spatially different testing areas (as discussed in Supplementary section S, Table T10). Accuracy metrics for Fold 1 (train and validation: India and Japan, test: Greece), Fold 2 (train and validation: India and Greece, test: Japan), and Fold 3 (train and validation: Greece and Japan, test: India) are included in Supplementary section Tables T11, T12 and T13 respectively. It was found that accuracy metrics of F1 and IoU were lower with higher False Negative Rate across all the Folds. For instance, the trained RF model for Fold 1 (train and validation: India and Japan, test: Greece), performs worse than the RF model trained on all the study sites and then tested on Greece test tiles (Fig. S37). Similarly, we found that trained RF models for Folds 2 and 3 perform worse than their corresponding RF model trained on all the study sites and then assessed on test tiles (Figs. S35 and S36). The primary reason of lower scores for each Fold is that the RF model was not trained on representative land cover of the flooded study site from where the test tile in obtained, thus, showing lower scores and higher FNR. In summary, we recommend training the RF model on representative land cover from flooded study sites from where the test tiles are obtained since we found that machine learning model perform worse if not trained on representative flooded samples. For example, if model is trained on India and Greece not on Japan flooded land cover, that model will perform worse than the one trained on representative flooded land cover from all the study sites.

The proposed flood index-based method is dependent on mechanism of SAR signal interactions with flooded areas. In relation to the multi-scale polarimetric spatial fusion approach (Q. Zhang and Hu, 2024), our method avoids complex segmentation and fusion pipelines by embedding Stokes-derived parameters directly into the FI, enabling robust mapping with simpler implementation and reduced computational cost. Similarly, in comparison with the hybrid Bayesian-GMM strategy (Surampudi & Kumar, 2024), our method is not dependent on full polarimetric SAR acquisitions; it operates effectively on dual-pol Sentinel-1 data, making it broadly applicable to operational flood monitoring. Furthermore, in comparison with the attention U-Net approach (Fakhri and Gkanatsios, 2025), our framework demonstrates better generalization across diverse geographic regions without requiring region-specific retraining, owing to its reliance on physical scattering mechanisms rather than learned spatial patterns (as discussed in Supplementary Section S, Table T10 about 3-fold cross-validation). Relative to the convolutional Siamese network (Ghasemian Sorboni et al., 2024) where careful loss function tuning is required across urban and non-urban floods, our method maintains consistent performance across different land-cover types and less sensitive to speckle noise. Compared to thresholding and fuzzy logic methods (Amitrano et al., 2024), which often struggle in heterogeneous areas due to assumptions of bimodal histograms and sensitivity to speckle, our methodology uses

multi-dimensional polarimetric features to separate water from low-backscatter non-water surfaces (e.g., asphalt, bare soil), reducing false alarms without manual thresholding. Unlike the dual-pol fuzzy union and intersection method (Kim et al., 2025), requiring iterative membership updates and defuzzification, our approach combines polarimetric information into a single feature vector for a supervised classifier, avoiding iterative refinement while maintaining interpretability and efficiency. Overall, the proposed FI with Random Forest offers clear physical interpretability, easy implementation, and higher accuracy in complex land-cover conditions, overcoming the limits of existing methods.

5. Conclusion

As floods have become more frequent and severe in recent years, especially affecting urban systems, there is a growing need for fast and scalable flood prediction methods to support emergency response and spatial planning. In this study, we introduce an index-based machine learning framework for flood detection using SAR polarimetric descriptors to detect flood water in mixed LULC environments representing urban and agriculture areas using Sentinel-1 data. For instance, we have used polarimetric descriptors of Degree of Polarization (DOP), which is considered as the 'anisotropy' of dual-pol data, and Linear Polarization Ratio (LPR). We develop a Flood Index (FI) utilizing Stokes parameters (DOP and LPR) and Eigenvalues to detect flooded urban and flooded vegetation for precise flood mapping. We train the machine learning model of Random Forest on the proposed Flood Index, and we compare its performance with Otsu and NDFI. We find that the Random Forest model trained on the proposed FI shows higher accuracy in flood detection across three study sites in Japan, India, and Greece. This is because the proposed FI uses both amplitude and phase of the radar signal, unlike intensity-only methods [NDFI and Otsu's (VH/VV)]; by capturing polarization state changes, the phase provides signal orientation and stability, for separating smooth flooded surfaces (stable phase, specular reflection) from rough land or vegetation (randomized phase), especially in mixed or vegetation areas. FI uses physically meaningful polarimetric descriptors (DOP, LPR, eigenvalues). The key contributions of our study are as follows:

- Our proposed FI is able to detect floods across different regions using radar signals based on physical scattering properties rather than relying on spatial patterns learned from specific training data.
- We design the FI to reduce SAR speckle noise through normalization, using ratios of pre- and during-flood Stokes parameters that help to reduce both common additive and multiplicative SAR speckle noise.
- The proposed Flood Index detects flood extents for events in India, Greece, and Japan encompassing varied land cover and land use type. However, we do not claim the global applicability of the proposed index until applied at more test sites, which is a future scope of this work.

This study shows the significance of Stokes parameters-based index for flood water identification and mapping using dual-polarized open-source Sentinel-1 SAR data. While several polarimetric decomposition techniques are based on either fully polarized or compact polarized data for flood identification tasks, our proposed index offers a simpler method for identifying floodwater since dual-polarized data is widely available. Alongside, this method looks forward to using data from the upcoming NASA-ISRO NISAR mission, which will offer improved and frequent observations for better flood monitoring in cities. These Earth observation resources provide critical, all-weather, day-and-night imaging capabilities that are essential for timely flood risk assessment and urban hazard monitoring.

Our recommendation for future work includes detailed Another direction for future research is to compare L-band ALOS-2 with dual-polarized C-band Sentinel-1 data in the flood affected areas using our proposed Flood Index.

CRediT authorship contribution statement

Ruma Adhikari: Writing – review & editing, Writing – original draft, Visualization, Validation, Software, Resources, Methodology, Investigation, Formal analysis, Data curation, Conceptualization. **Alok Bhardwaj:** Writing – review & editing, Supervision, Resources, Project administration, Funding acquisition.

Data and code availability statement

Research data and code, as described in this document, will be made available upon reasonable request. Request for access to the data should be directed to the corresponding author.

Declaration of generative AI and AI-assisted technologies in the writing process

During the preparation of this work the authors used Claude.ai in order to grammar check. After using this tool/service, the authors reviewed and edited the content as needed and take full responsibility for the content of the publication.

Declaration of competing interest

The authors declare that they have no known competing financial interests or personal relationships that could have appeared to influence the work reported in this paper.

Acknowledgments

The research work is supported by the Science and Engineering Research Board (SERB) of India (Research Project no. SER-1772-CED (File No. SRG/2021/001706) registered in SRIC, IIT Roorkee) and National Geographic Society (Research Project no. NGF-1640-CED (File registered in SRIC, IIT Roorkee). The authors acknowledge the European Space Agency (ESA) for the open-source software provided by the PolSARpro (The Polarimetric SAR Data Processing and Educational Tool) and SNAP (Sentinel Application Platform) projects. Authors also thank the "Joint Research Centre - by European Commission" for the open access "JRC Global Surface Water Dataset".

Appendix A. Supplementary data

Supplementary data to this article can be found online at https://doi.org/10.1016/j.jenvman.2025.128208.

Data availability

Data will be made available on request.

References

Adhikari, R., 2021. Mapping of flooded heritage structures using SAR polarimetry and Google Earth engine. EGU General Assembly Conference Abstracts. https://doi.org/10.5194/egusphere-egu21-13978. EGU21–13978. https://ui.adsabs.harvard.edu/link_gateway/2021EGUGA..2313978A/.

Adhikari, R., Bhardwaj, A., Khati, U., 2022. Investigation of long-lasting damage due to Hagibis flood using SAR polarimetry and ALOS-2 data in Japan. AGU Fall Meeting Abstracts 2022. H41B–04. https://doi.org/2022AGUFM.H41B..04A.

Adhikari, R., Tsutsumida, N., Bhardwaj, A., 2023. An index-based flood mapping using Stokes parameters of multitemporal SAR images: 2019 Hagibis flood event of Ibaraki, Japan. In: IGARSS 2023 - 2023 IEEE International Geoscience and Remote Sensing Symposium, pp. 7194–7197. https://doi.org/10.1109/IGARSS52108.2023.10281581.

Amitrano, D., Di Martino, G., Di Simone, A., Imperatore, P., 2024. Flood detection with SAR: a review of techniques and datasets. Remote Sens. 16 (4), 1–38. https://doi.org/10.3390/rs16040656.

Breiman, L., Friedman, J.H., Olshen, R.A., Stone, C.J., 1984. Classification and regression trees. Biometrics 40, 874. https://api.semanticscholar.org/CorpusID:29458883.
Brisco, B., Schmitt, A., Murnaghan, K., Kaya, S., Roth, A., 2013. SAR polarimetric change detection for flooded vegetation. International Journal of Digital Earth 6 (2), 103–114. https://doi.org/10.1080/17538947.2011.608813.
CBS, 2023. Historic flooding event" in Greece dumps more than 2 feet of rain in just a few hours. https://www.cbsnews.com/news/greece-historic-flooding-more-than-2-feet-of-rain-in-just-a-few-hours/.
Cian, F., Marconcini, M., Ceccato, P., 2018. Normalized Difference Flood Index for rapid flood mapping: taking advantage of EO big data. Remote Sensing of Environment 209 (February), 712–730. https://doi.org/10.1016/j.rse.2018.03.006.
Portner, H.O., Roberts, D.C., Tignor, M., Poloczanska, E.S., Mintenbeck, K., Alegria, A., Craig, M., Langsdorf, S., Loschke, S., Moller, V., Okem, A., Rama, B., 2022. IPCC, 2022: Climate Change 2022: Impacts, Adaptation and Vulnerability. In: Sixth Assessment Report of the Intergovernmental Panel on Climate Change (Issue August). https://doi.org/10.1017/9781009325844.
CRED. (2020). https://cred.be/sites/default/files/adsr_2019.pdf.
Das, S., Alexander, J., Ishiwatari, M., Komino, T., Shaw, R., 2020. Lessons from Hagibis: Learning to Cope with Intensifying Disasters in the Age of New Normal. Church World Service Japan, pp. 2–3.
Dasgupta, A., Grimaldi, S., Ramsankaran, R., Pauwels, V.R.N., Walker, J.P., Chini, M., Hostache, R., Matgen, P., 2018. Flood mapping using Synthetic Aperture Radar sensors from local to global scales, 55–77. https://doi.org/10.1002/9781119217886.ch4.
Elkharrouba, E., Sekertekin, A., Fathi, J., Tounsi, Y., Bioud, H., Nassim, A., 2022. Surface soil moisture estimation using dual-Polarimetric Stokes parameters and backscattering coefficient. Remote Sens. Appl.: Society and Environment 26 (December 2021), 100737. https://doi.org/10.1016/j.rsase.2022.100737.
Ermagun, A., Smith, V., Janatabadi, F., 2024. High urban flood risk and no shelter access disproportionally impacts vulnerable communities in the USA. Commun. Earth Environ. 5 (1). https://doi.org/10.1038/s43247-023-01165-x.
Fakhri, F., Gkanatsios, I., 2025. Quantitative evaluation of flood extent detection using attention U-Net case studies from Eastern South Wales Australia in March 2021 and July 2022. Sci. Rep. 15 (1), 1–14. https://doi.org/10.1038/s41598-025-92734-x.
Farr, T.G., Rosen, P.A., Caro, E., Crippen, R., Duren, R., Hensley, S., Kobrick, M., Paller, M., Rodriguez, E., Roth, L., Seal, D., Shaffer, S., Shimada, J., Umland, J., Werner, M., Oskin, M., Burbank, D., Alsdorf, D., 2007. The shuttle radar topography mission, 2005, 1–33. https://doi.org/10.1029/2005RG000183.1.INTRODUCTION.
Felix, I.K., Marino, A., Silva, T.S.F., Bovolo, I., Berardi, A., Neil, C., 2024. Mapping floods using SAR polarimetry in Imola, Italy. IGARSS 2024 - 2024 IEEE International Geoscience and Remote Sensing Symposium 10799–10802. https://doi.org/10.1109/igarss53475.2024.10640708.
FloodList, 2023. FloodList. https://floodlist.com/asia/india-floods-delhi-july-2023.
Fu, B., Xie, S., He, H., Zuo, P., Sun, J., Liu, L., Huang, L., Fan, D., Gao, E., 2021. Synergy of multi-temporal polarimetric SAR and optical image satellite for mapping of marsh vegetation using object-based random forest algorithm. Ecol. Indic. 131, 108173. https://doi.org/10.1016/j.ecolind.2021.108173.
Garg, S., Dasgupta, A., Motagh, M., Martinis, S., Selvakumaran, S., 2024. Unlocking the full potential of Sentinel-1 for flood detection in arid regions. Remote Sensing of Environment 315 (September), 114417. https://doi.org/10.1016/j.rse.2024.114417.
Ghasemian Sorboni, N., Wang, J., Najafi, M.R., 2024. Urban flood mapping using Sentinel-1 and RADARSAT Constellation Mission image and convolutional Siamese network. In: Natural Hazards, vol.120. Springer, Netherlands. https://doi.org/10.1007/s11069-024-06434-2. Issue 6.
Gou, S., Qiao, X., Zhang, X., Wang, W., Du, F., 2014. Eigenvalue analysis-based approach for POL-SAR image classification. IEEE Trans. Geosci. Rem. Sens. 52 (2), 805–818. https://doi.org/10.1109/TGRS.2013.2244096.
Guissard, A., 1994. Mueller and Kennaugh Matrices in Radar polarimetry. IEEE Trans. Geosci. Rem. Sens. 32 (3), 590–597. https://doi.org/10.1109/36.297977.
Halder, B., Barman, S., Banik, P., Das, P., Bandyopadhyay, J., Tangang, F., Shahid, S., Pande, C.B., Al-Ramadan, B., Yaseen, Z.M., 2023. Large-scale flood hazard monitoring and impact assessment on landscape: representative case study in India. Sustainability 15 (14). https://doi.org/10.3390/su151411413.
Karanam, V., Motagh, M., Garg, S., Jain, K., 2021. Multi-sensor remote sensing analysis of coal fire induced land subsidence in Jharia Coalfields, Jharkhand, India. Int. J. Appl. Earth Obs. Geoinf. 102 (February), 102439. https://doi.org/10.1016/j.jag.2021.102439.
Kazemi Garajeh, M., Weng, Q., Hossein Haghi, V., Li, Z., Kazemi Garajeh, A., Salmani, B., 2022. Learning-based methods for detection and monitoring of shallow flood-affected areas: impact of shallow-flood spreading on vegetation density. Can. J. Rem. Sens. 48 (4), 481–503. https://doi.org/10.1080/07038992.2022.2072277.
Kim, S.Y., Lee, Y., Park, S.E., 2025. On flood detection using dual-polarimetric SAR observation. Remote Sens. 17 (11), 1–19. https://doi.org/10.3390/rs17111931.
Kumar, K., Chowdhury, A., Bhardwaj, A., 2025. Investigation of physical causes for long-term deformation at urbanized towns in Indian himalayas: a case study for Joshimath, Uttarakhand. Natural Hazards. https://doi.org/10.1007/s11069-025-07608-2.
Mandal, D., Kumar, V., Ratha, D., Dey, S., Bhattacharya, A., Lopez-Sanchez, J.M., McNairn, H., Rao, Y.S., 2020. Dual polarimetric radar vegetation index for crop growth monitoring using sentinel-1 SAR data. Remote Sensing of Environment 247 (January), 111954. https://doi.org/10.1016/j.rse.2020.111954.
Mandal, D., Vaka, D.S., Bhogapurapu, N.R., Vanama, K.S.K., Kumar, V., Rao, Y.S., Bhattacharya, A., 2019. Sentinel-1 SLC preprocessing workflow for polarimetric applications: a generic practice for generating dual-pol covariance matrix elements in SNAP S-1 Toolbox. Preprints, November, 2019110393. https://doi.org/10.20944/preprints201911.0393.v1.
Mason, D.C., Giustarini, L., Garcia-Pintado, J., Cloke, H.L., 2014. Detection of flooded urban areas in high resolution Synthetic Aperture Radar images using double scattering. Int. J. Appl. Earth Obs. Geoinf. 28 (1), 150–159. https://doi.org/10.1016/j.jag.2013.12.002.
Mehedi, M. A. Al, Smith, V., Kremer, P., 2022. Comparing urban flood dynamics using SAR imagery and Google Earth Engine: case studies in dhaka and houston. In: AGU Fall Meeting Abstracts, vol 2022, pp. H42F–1363.
MLIT, 2021. Ministry of land, infrastructure, Transport and Tourism (MLIT) Japan, 0–17. https://www.mlit.go.jp/en/statistics/content/001442571.pdf.
Nayak, S., Takemi, T., 2023. Statistical analysis of the characteristics of typhoons approaching Japan from 2006 to 2019. Geomat. Nat. Hazards Risk 14 (1). https://doi.org/10.1080/19475705.2023.2208722.
NVC, 2008. National vegetation classification. Environ. Manag. 703–715, 2008 (February). http://www.ncbi.nlm.nih.gov/pubmed/12180183.
Otsu, N., 1979. Threshold selection method from gray-level histograms. IEEE Trans. Syst. Man Cybern. SMC-9 (1), 62–66. https://doi.org/10.1109/tsmc.1979.4310076.
Pekel, J., Cottam, A., Gorelick, N., Belward, A.S., 2016. Letter. Nature Publishing Group. https://doi.org/10.1038/nature20584.
Phy, S.R., Sok, T., Try, S., Chan, R., Uk, S., Hen, C., Oeurng, C., 2022. Flood hazard and management in Cambodia: a review of activities, knowledge gaps, and research direction. Climate 10 (11), 1–15. https://doi.org/10.3390/cli10110162.
Pierdicca, N., Pulvirenti, L., Boni, G., Squicciarino, G., Chini, M., 2017. Mapping flooded vegetation using COSMO-SkyMed: comparison with polarimetric and optical data over rice fields. IEEE J. Sel. Top. Appl. Earth Obs. Rem. Sens. 10 (6), 2650–2662. https://doi.org/10.1109/JSTARS.2017.2711960.
Pirrone, D., Pirrone, D., Bovolo, F., Bruzzone, L., 2020. A novel framework based on polarimetric change vectors for unsupervised multiclass change detection in dual-pol intensity SAR images. IEEE Trans. Geosci. Rem. Sens. 58 (7), 4780–4795. https://doi.org/10.1109/TGRS.2020.2966865.
Plank, S., Jüssi, M., Martinis, S., Twele, A., 2017. Mapping of flooded vegetation by means of polarimetric sentinel-1 and ALOS-2/PALSAR-2 imagery. Int. J. Rem. Sens. 38 (13), 3831–3850. https://doi.org/10.1080/01431161.2017.1306143.
Pulvirenti, L., Chini, M., Pierdicca, N., Boni, G., 2016. Use of SAR data for detecting floodwater in urban and agricultural areas: the role of the interferometric coherence. IEEE Trans. Geosci. Rem. Sens. 54 (3), 1532–1544. https://doi.org/10.1109/TGRS.2015.2482001.
Schumann, G.J., 2024. Breakthroughs in satellite remote sensing of fl oods. April, 1–10. https://doi.org/10.3389/frsen.2023.1280654.
Sghaier, M.O., 2018. Flood extent mapping from time-series SAR images based on texture analysis and data fusion, 1–30. https://doi.org/10.3390/rs10020237.
Skolnik, M.I., 2014. Introduction to radar systems. In: second editionEcohouse.
Soudagar, R., Chowdhury, A., Bhardwaj, A., 2025. Enhanced large-scale flood mapping using data-efficient unsupervised framework based on morphological active contour model and single Synthetic Aperture Radar image. J. Environ. Manag. 380 (124836), 124836. https://doi.org/10.1016/j.jenvman.2025.124836.
Subbarayan, S., Youssef, Y.M., Singh, L., Dąbrowska, D., Alarifi, N., Ramsankaran, R.A.A. J., Visweshwaran, R., Saqr, A.M., 2025. Soil and water assessment tool-based prediction of runoff under scenarios of land use/land cover and climate change across Indian agro-climatic zones: implications for sustainable development goals. Water (Switzerland) 17 (3). https://doi.org/10.3390/w17030458.
Surampudi, S., Kumar, V., 2024. Hybrid Naïve Bayes Gaussian mixture models and SAR polarimetry based automatic flooded vegetation studies using PALSAR-2 data. Remote Sens. Appl.: Society and Environment 36 (February), 101361. https://doi.org/10.1016/j.rsase.2024.101361.
Tanim, A.H., McRae, C.B., Tavakol-davani, H., Goharian, E., 2022. Flood detection in urban areas using satellite imagery and machine learning. Water (Switzerland) 14 (7). https://doi.org/10.3390/w14071140.
Tavakoli, M., Motlagh, Z.K., Dąbrowska, D., Youssef, Y.M., Đurin, B., Saqr, A.M., 2025. Harnessing AHP and fuzzy scenarios for resilient flood management in arid environments: challenges and pathways toward sustainability. Water (Switzerland) 17 (9). https://doi.org/10.3390/w17091276.
Tay, C.W.J., Yun, S.H., Chin, S.T., Bhardwaj, A., Jung, J., Hill, E.M., 2020. Rapid flood and damage mapping using Synthetic Aperture Radar in response to Typhoon Hagibis, Japan. Sci. Data 7 (1), 1–9. https://doi.org/10.1038/s41597-020-0443-5.
Times, T.E., 2025. Bangalore rain crisis leaves five dead, several without electricity or relief in Sai Layout and other areas. ET Online. https://economictimes.indiatimes.com/news/bengaluru-news/bengalurus-rain-crisis-city-records-heaviest-deluge-since-2017-leaves-five-dead-hundreds-of-homes-submerged-in-indias-it-capital/printarticle/121303422.cms.
Tse-Hei Lee, J., 2020. Asia. The Oxford Handbook of Christmas, pp. 511–521. https://doi.org/10.1093/oxfordhb/9780198831464.001.0040.
Tsyganskaya, V., 2019. Detection of Temporarily Flooded Vegetation Using Time Series of Dual Polarised C-Band Synthetic Aperture Radar Data. September.
Wang, H., Magagi, R., Goïta, K., Trudel, M., McNairn, H., Powers, J., 2019. Crop phenology retrieval via polarimetric SAR decomposition and Random Forest algorithm. Remote Sensing of Environment 231 (April), 111234. https://doi.org/10.1016/j.rse.2019.111234.
Zhang, B., Wdowinski, S., Gann, D., Hong, S.H., Sah, J., 2022. Spatiotemporal variations of wetland backscatter: the role of water depth and vegetation characteristics in

Sentinel-1 dual-polarization SAR observations. Remote Sensing of Environment 270 (July 2021), 112864. https://doi.org/10.1016/j.rse.2021.112864.
Yamaguchi, Y., 2020. Polarimetric SAR Imaging: Theory and Applications, 1st Edition. CRC Press. https://doi.org/10.1201/9781003049753.
Zhang, Q., Hu, X., 2024. Urban flood mapping by fully mining and adaptive fusion of the polarimetric and spatial information of Sentinel-1 images. Int. J. Appl. Earth Obs. Geoinf. 135 (October), 104251. https://doi.org/10.1016/j.jag.2024.104251.